Nano Research

Open Access

Research Article

Real-time observation and synchronous nanomanipulation platform based on microlens and atomic force microscopy coupling

Tianyao Zhang[1,2], Haibo Yu[3,4], Guoqiang Gu[1], Jienan Shen[1], Huitao Zhang[1], Zitong Yu[1], Shi Hu[1], and Hui Yang[1,2] ✉

[1] *Institute of Biomedical and Health Engineering, Shenzhen Institutes of Advanced Technology, Chinese Academy of Sciences, Shenzhen 518055, China*
[2] *Key Laboratory of Biomedical Imaging Science and System, Chinese Academy of Sciences; State Key Laboratory of Biomedical Imaging Science and System, Shenzhen 518055, China*
[3] *State Key Laboratory of Robotics, Shenyang Institute of Automation, Chinese Academy of Sciences, Shenyang 110016, China*
[4] *Institutes for Robotics and Intelligent Manufacturing, Chinese Academy of Sciences, Shenyang 110016, China*

Cite this article: *Nano Research*, **2025**, *18*, 94907397. https://doi.org/10.26599/NR.2025.94907397

ABSTRACT: Nanomanipulation based on atomic force microscopy (AFM) is widely used in various fields, including nanoparticle assembly, nanostructure construction, and semiconductor device manufacturing. However, a challenge remains in the lack of nanoscale visual feedback, which limits operational efficiency and accuracy. Here, we present a method for nanomanipulation under the visual guidance of real-time super-resolution imaging. The method involves coupling a microlens to the end of a conventional AFM probe cantilever and depositing a diamond tip onto the surface of the microlens using focused ion beam (FIB). The resulting microlens-AFM probe enhances the imaging resolution of traditional AFM optical systems, providing super-resolution capability with a multiple 3× increase in optical imaging magnification and enabling synchronous imaging and manipulation of silver nanowires with a characteristic size of 200 nm. This advancement bridges the key gap in AFM-based nanomanipulation by providing *in-situ*, real-time, non-destructive, and ultra-high-resolution visual feedback. This technology has the potential to provide new methods and key technologies for research in a wide range of applications, including nanorobots, nanoobservation, nanomanipulation, and manufacturing.

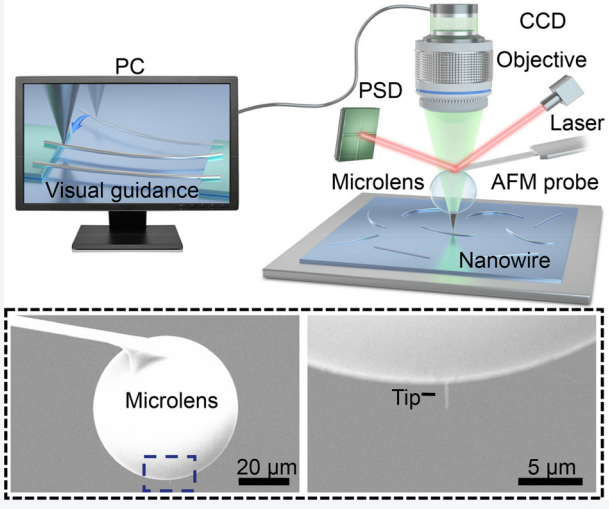

KEYWORDS: microlens, atomic force microscopy (AFM), optical super-resolution imaging, nanomanipulation, microsphere

1 Introduction

The development of efficient, sensitive, and adaptable nanomanipulation systems holds great potential in advancing the construction of nanostructures, biomedical applications, and semiconductor device manufacturing. Since the invention of the atomic force microscopy (AFM) by Binnig in 1986 [1], this technology has emerged as a powerful tool for atomic-level high-resolution imaging, enabling morphology detection, nanoprocessing, and nanomanipulation across various materials and samples in diverse environments [2–6]. Despite its dual functionality as an imaging and manipulation tool [7], AFM's inability to perform these tasks simultaneously hinders real-time feedback during manipulation, leading to inefficiencies and challenges in achieving precise results. The reliance on cantilever contact for imaging and the sequential imaging-design-manipulation-imaging workflow in the typical nanomanipulation procedure further exacerbates the issues of low efficiency and lack of feedback information for real-time adjustment of the operation process to obtain accurate operation results, underscoring the urgent need for super-resolution online visual feedback to enhance the accuracy, stability, and operational efficiency of AFM-based micro/nano manipulation.

Current micro/nanoscale imaging methodologies encompass electron microscopy (EM) [8], scanning probe microscopy (SPM)

Received: January 8, 2025; **Revised:** March 6, 2025
Accepted: March 24, 2025

✉Address correspondence to hui.yang@siat.ac.cn

[9], and optical microscopy (OM) [10], each with distinct advantages and limitations. SPM employs nanoscale tips to scan points on a sample surface, enabling the acquisition of images depicting its surface topography. However, it is incapable of performing manipulation and imaging simultaneously. EM, on the other hand, utilizes extremely short wavelength electron beams for imaging. Micro/nanoscale manipulation systems based on EM operate within a vacuum chamber, which restricts the type of samples that can be manipulated and necessitates sample preparation. This preparation process may introduce nonexistent structures or cause sample defects, and the irradiation of the electron beam can also inflict radiation damage to the manipulated sample. Both of these imaging methods rely on serial point scanning, posing challenges in achieving real-time imaging and studying dynamic behaviors, such as object movement and changes, during micro/nanoscale manipulation. In contrast, OM boasts advantages such as suitability for live imaging, penetrability, true color imaging, real-time feedback, low cost, and low maintenance, yet it is inherently diffraction-limited, restricting its spatial resolution.

As the cornerstone of microscopic observation, OM plays a pivotal role in surface science, materials science, and life sciences. However, the diffraction limit imposed by the wavelength of light and the system's relative aperture, as described by Abbe's theory, restricts the spatial resolution of classical optical systems. To overcome this limitation, researchers have developed super-resolution optical microscopy techniques, including photo-activated localization microscopy (PALM) [11, 12], stochastic optical reconstruction microscopy (STORM) [13, 14], and stimulated emission depletion (STED) [15, 16]. While these methods have achieved remarkable imaging resolutions, their reliance on fluorescent labeling and long imaging times hinder their suitability for real-time, non-destructive, and label-free imaging during synchronous nanomanipulation.

In contrast, super-resolution imaging based on microlens represents an emerging near-field optical imaging technology that promises to overcome these challenges [17–22]. Studies have demonstrated the ability of microlens to achieve strong near-field focusing and amplification, surpassing the optical diffraction limit at low intensities. Multiple theories have been proposed to explain the super-resolution imaging mechanism of microlenses [23, 24], including evanescent field enhancement, photonic nanojets, and plasmon resonance. Our findings suggest that the microlens achieves super-resolution primarily by interacting with evanescent waves near the sample surface. These waves, which carry subwavelength details, are converted into propagating waves through the microlens. This conversion enables the optical system to resolve features beyond the diffraction limit. In 2009, Lee et al. demonstrated that self-assembled spherical immersion lenses could achieve strong near-field focusing and amplification, surpassing the optical diffraction limit at low intensity. They clearly imaged and resolved individual metal stripes with a spacing of 220 nm [25]. In 2011, Wang et al. introduced silica microspheres as optical superlens into traditional optical microscopy, proposing a new nanoscopy technique that achieves imaging with a resolution of 50 nm [26]. Subsequently, researchers immersed high refractive index microspheres in different liquids for imaging and analysis, finding that barium titanate glass microspheres immersed in water environments could achieve good imaging results [27]. Yan et al. combined microlens-based super-resolution optical imaging technology with confocal microscopy, further increasing the imaging resolution to 25 nm [28]. In the field of life sciences, Yang et al. successfully observed subcellular organelles such as centromeres, mitochondria, and chromosomes using microsphere-based fluorescence imaging [29]. In addition, imaging of adenovirus [30], mouse fibroblasts, and cancer cell nuclei under white light illumination has also been achieved [31]. To more accurately control the imaging position and expand the imaging range, researchers have employed chemical drivers [32], acoustic fluids [33, 34], and optical tweezers [35, 36] for microsphere scanning imaging. Alternatively, by fixing microlenses to capillary glass tubes [37], AFM probes [38, 39], or objective lenses [40], large-scale scanning imaging is achieved through a three-dimensional (3D) mobile platform [32, 41, 42]. Notably, Wang et al. innovatively coupled microspheres with the cantilever of an AFM probe, achieving controllable and stable large-scale scanning splicing super-resolution imaging and white light fluorescence co-imaging for both biological and non-biological samples [43]. This demonstrates the strong potential for combining the functionalities of superlens microscopy and AFM. The super-resolution optical imaging method based on microlens is characterized by its real-time, non-destructive, and label-free nature, making it suitable for real-time visual feedback during manipulation.

In this study, we present an integrated method combining super-resolution optical imaging based on microlens with AFM manipulation. By coupling a microlens to the end of a conventional AFM probe cantilever and depositing a diamond tip using focused ion beam (FIB), we have designed and fabricated a microlens-AFM probe. This probe enables real-time super-resolution imaging visual guidance during manipulation, allowing for synchronous imaging and precise control of feature-sized targets down to tens of nanometers. The AFM system controls the operating force, speed, and trajectory, while the coupling of the microlens and AFM optical path system provides real-time feedback, improving the efficiency and accuracy of AFM-based nanomanipulation.

2 Experimental

2.1 Experimental equipment

To enhance the imaging resolution and magnification of commercial AFM, we introduced microsphere-based high-resolution optical imaging technology using a custom-designed microlens-AFM probe (Dimension Icon, Bruker, USA). This setup facilitated synchronous imaging and magnification of silver nanowires under visual guidance. The customized microlens-AFM probe was fabricated by coupling a 60 μm diameter silica microsphere to a commercial probe and depositing a diamond tip with a length of approximately 2 μm using FIB technology. The probe had mechanical parameters of a nominal spring constant of 42 N/m and a resonant frequency of 50–120 kHz, enabling optical imaging in an air environment. Stable imaging and manipulation conditions were ensured by adjusting the distance and interaction force between the sample and the microlens through the AFM system's control feedback mechanism. Nanomanipulation of silver nanowires with diameters of 200 and 80 nm was performed in air using nanomen mode. AFM scanning imaging of square areas ranging from 20 to 40 μm was conducted on the sample surface using tapping mode with a scanning rate of 0.3 Hz.

2.2 Sample preparation

Silver nanowires with diameters of 200 and 80 nm (NN-D-125, Nanochem, China) were diluted with water to a concentration of approximately 2 × 10^{-3} mg/mL. The suspension was then thoroughly shaken and sonicated. The silicon substrate was cleaned with plasma water and anhydrous ethanol and dried with nitrogen gas. Subsequently, the silver nanowire suspension was dropped and dispersed onto the surface of the silicon substrate and left to dry for at least 5 h before the experiment.

2.3 Image analysis

AFM images were analyzed using Nanoscope Analysis 1.9 (Bruker, USA). Optical images were captured by an AFM optical system camera at a frame rate of 30 Hz and a resolution of 640 × 480. MATLAB or Visio software was used to crop and stitch the optical imaging results of large-area scanning based on the microlens, obtaining high-resolution optical images over a large area. The intensity of the cross-sectional profile information extracted from AFM scanning imaging results was normalized. Scanning electron microscopy (SEM) images were captured using a Zeiss EVO MA10 scanning electron microscope.

3 Results and discussion

3.1 Super-resolution observation and synchronous nanomanipulation system

Based on the Abbe's diffraction limit theory, the imaging resolution of traditional optical microscopy cannot distinguish two objects located less than $\lambda/2$ NA. The principle of super-resolution imaging based on microlens is related to evanescent waves, and microlens can convert evanescent waves carrying subwavelength information of the sample into propagating waves, thereby achieving super-resolution imaging (Fig. S1 in the Electronic Supplementary Material (ESM)). Figure 1(a) illustrates the schematic of the experimental setup for super-resolution observation and synchronous nanomanipulation. While the control method of the microlens is mainly used to assist in scanning imaging, its potential application in nanomanipulation has yet to be fully explored. In contrast to other microlens control strategies, affixing the microlens to an AFM probe offers precise control in the z-direction, conferring distinct advantages in nanomanipulation tasks. Furthermore, the integration of both the microlens and AFM probe within the near-field region of the sample facilitates the interactive optimization of the manipulation and imaging system. The experimental system comprises an AFM, a super-resolution optical imaging pathway, and a custom-designed microlens-AFM probe. By securing the microlens to the cantilever end of a traditional commercial AFM probe and depositing the probe tip on the lower surface of the microlens facing the sample, this method integrates microlens-based imaging technology into a standard AFM system. The combination of the microlens coupled to the AFM probe, alongside the reflective optical imaging pathway of the AFM, achieves enhanced imaging resolution and virtual image amplification. This optical imaging technique boasts real-time, non-destructive, and high-resolution capabilities, enabling the acquisition of sample position and shape prior to manipulation, real-time super-resolution imaging visual guidance during manipulation, and confirmation of the final manipulation effect through imaging. Prior to nanomanipulation, the force, speed, and trajectory can be pre-set based on the sample and adjusted in real-time using visual feedback images, leveraging the AFM system's

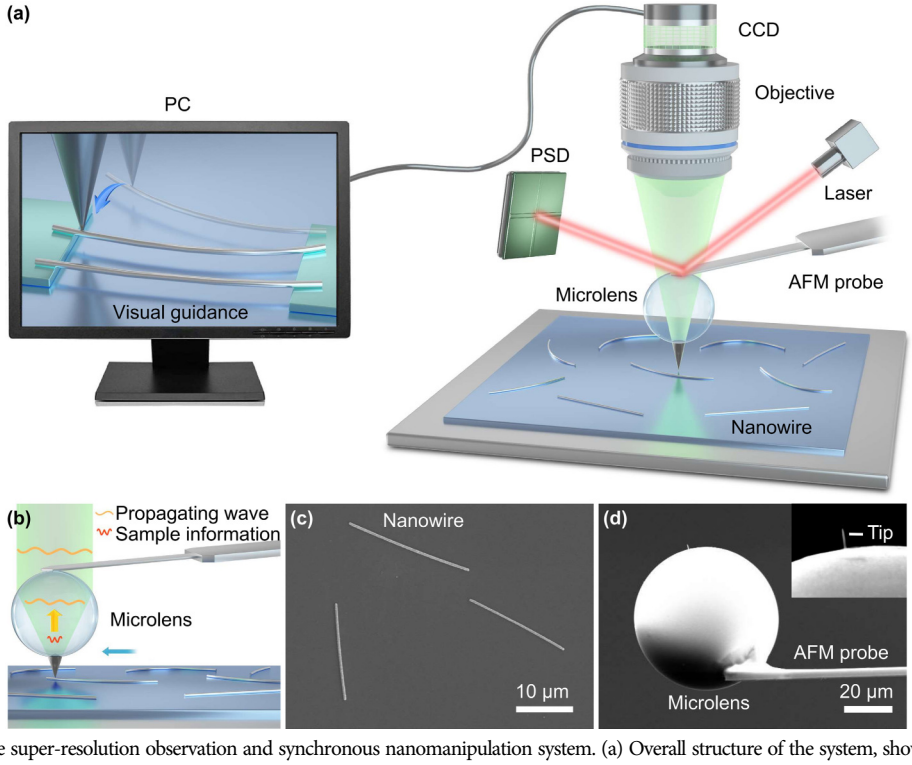

Figure 1 Schematic of the super-resolution observation and synchronous nanomanipulation system. (a) Overall structure of the system, showing the microlens fixed to the end of a traditional commercial AFM probe cantilever with the probe tip deposited on the lower surface of the microlens. The customized microlens-AFM probe introduces microlens-based imaging technology into the AFM system, enabling synchronous imaging and manipulation of samples. (b) Schematic diagram illustrating the principles of manipulation and imaging. (c) SEM image of silver nanowires with a characteristic size of 200 nm. (d) SEM image of the customized microlens-AFM probe.

distance or interaction force control mechanism. To optimize imaging and manipulation, the distance between the microlens-AFM probe and the sample is fine-tuned by adjusting the amplitude setting point in the parameter controls. During scanning and manipulation, real-time vertical feedback from the scanner and feedback system ensures a constant microlens-sample distance. This feedback mechanism stabilizes imaging conditions and enhances manipulation precision. This approach achieves synchronous imaging and manipulation of samples with feature sizes down to 100 nm, thereby enhancing the efficiency and accuracy of AFM-based nanomanipulation.

3.2 Design and fabrication of the microlens-AFM probe

To incorporate microlens-based optical imaging into the AFM system, a novel end effector for nanomanipulation and near-field imaging, termed the microlens-AFM probe, was designed and fabricated. The fabrication process involved fixing a silica microsphere (50–60 μm diameter, refractive index of 1.46 for air immersion imaging) to a commercial AFM probe using ultraviolet-curable glue (NOA63, Edmund Optics). This was achieved by positioning the AFM probe, pre-coated with ultraviolet-curable glue, on a high-precision 3D displacement platform and gradually approaching a coupling microsphere until gentle contact was established.

To meticulously control the glue volume and minimize optical path interference, a capillary glass tube with a tip inner diameter of approximately 1 μm was employed to dispense the glue onto the AFM probe, guided by a precision 3D manual displacement platform under a commercial optical microscope (shown in Fig. 2(a)). This ensured that the optical imaging performance of the microlens remained unimpaired. Subsequently, a 100 W halogen lamp was used to irradiate the assembly for over 30 min, effectively curing the glue and fostering a stable coupling between the microlens and the AFM probe cantilever. Notably, the microsphere was positioned at the cantilever's edge, ensuring that the surface optical path area obscured by the cantilever and glue comprised less than 20% of the microsphere, optimizing optical accessibility. It is worth noting that the microsphere's diameter and refractive index can be selectively tailed to accommodate varying imaging requirements, such as field of view, resolution, and the specific environment of the sample under manipulation. This versatility underscores the probe's adaptability and potential for diverse applications.

Subsequently, a diamond tip was deposited on sample-facing surface of the microlens using FIB technology, with dimensions tailored to the sample characteristics while ensuring the microlens-sample distance fell within the optical imaging working distance. The diameter, height, and position of the tip were tailored to the characteristics of the sample to be manipulated, while ensuring the microlens-sample distance fell within the optical imaging working distance. Figures 2(b) and 2(c) present the SEM characterization of the microlens-AFM probe, showcasing a microlens diameter of 57 μm, a deposited tip height of ~ 1.7 μm, a base diameter of 250 nm, and a tip diameter less than 20 nm.

3.3 Optical numerical analysis of the microlens-AFM probe

The optical imaging performance of the microlens is related to the focusing characteristics of the photonic nanojet (PNJ) formation. In order to analyze the influence of the probe cantilever and deposition tip on the microlens' optical properties, an optical simulation model was constructed. A plane wave with a peak wavelength of λ = 550 nm is incident from top to bottom along the Z-axis, the microlens-AFM probe operates in an air environment (refractive index n_1 = 1), with the Si-doped cantilever beam (n_2 = 3.42), transparent silica microlens (n_3 = 1.5, 60 μm diameter), and diamond tip (n_4 = 2.4, 2 μm height, 250 nm base diameter, 10 nm tip diameter) included in the model. The intensity distribution of the light field in the model was simulated and analyzed using Lumeric finite difference time domain (FDTD) simulation software, as shown in Fig. 3.

The simulation results of the intensity distribution in the x–z plane of the microlens-AFM probe are shown in Figs. 3(a)–3(h). Figure 3(a) depicts the result of a single microlens without the inclusion of a cantilever and a deposition tip. The incident plane wave produces PNJ on the shaded surface under the focusing of the microlens. These results are used as a benchmark to assess the impact of the tip and cantilever on the focusing characteristics and optical imaging of the microlens. Figure 3(b) illustrates the light field distribution without a cantilever but with the addition of a

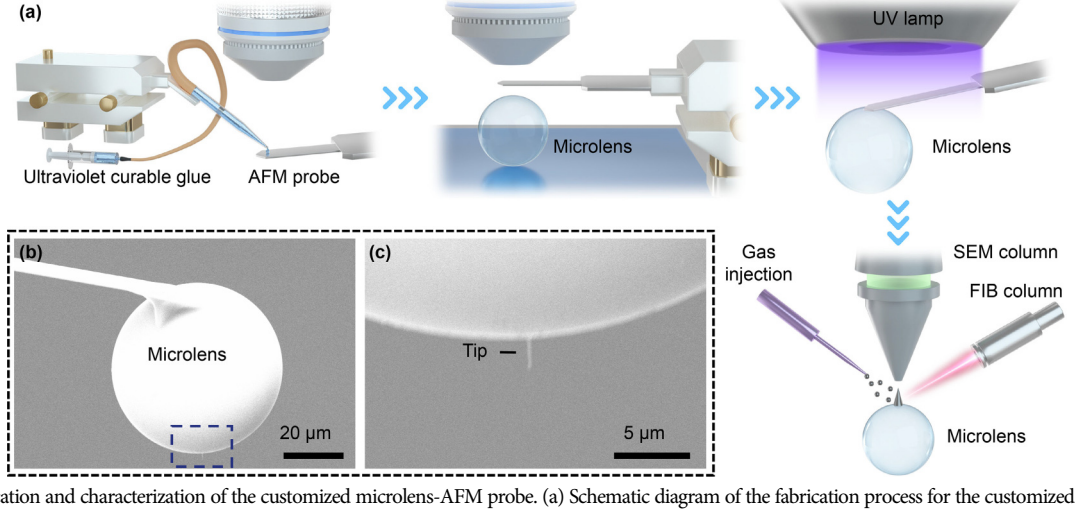

Figure 2 Fabrication and characterization of the customized microlens-AFM probe. (a) Schematic diagram of the fabrication process for the customized microlens-AFM probe. (b) SEM image of the customized microlens-AFM probe, showing a coupled microlens with a diameter of 57 μm and a deposited tip with a height of ~ 1.7 μm. (c) Expanded view of the SEM image in (b), providing a closer look at the probe's features.

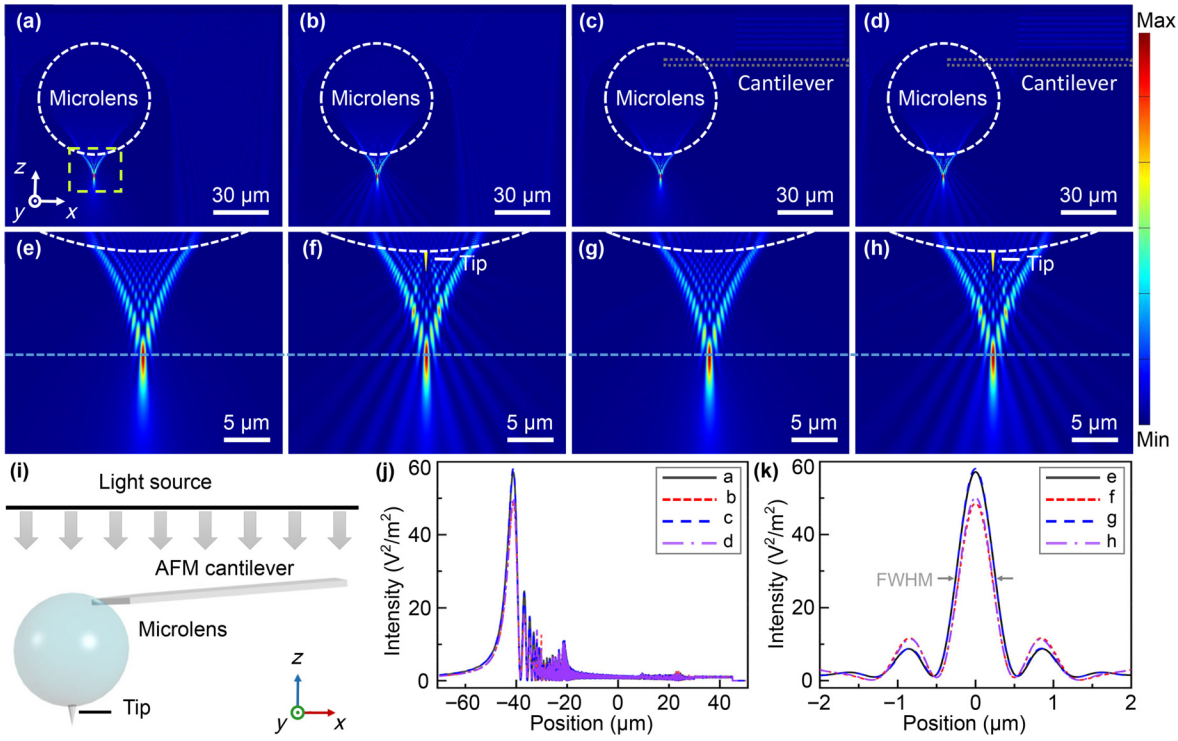

Figure 3 Optical numerical analysis of microlens-AFM probe via FDTD simulation. (a)–(d) Simulation results of light field intensity distribution: (a) single microlens, (b) microlens with a deposited tip, (c) microlens with a cantilever, and (d) microlens-AFM probe. Note: The microlens diameters are 60 μm in (a)–(d). (e)–(h) Expanded views of (a)–(d). (i) Simulation schematic diagram of the microlens-AFM probe. (j) Light field intensity distribution along the *z*-axis of the microlens in (a)–(d). (k) Light field intensity distribution along the *x*-axis of the microlens in (a)–(d).

deposited tip, showcasing the local light field interference effects introduced by the tip. Figures 3(c) and 3(d) exhibit the simulation results for the inclusion of a cantilever without a tip and with both a cantilever and a tip, respectively. By examing Figs. 3(e)–3(k), the focusing characteristics of the microlens can be more intuitively observed. The deposition of the tip leads to a minor reduction in the maximum intensity of PNJ, yet there are no substantial changes in the focal position (f) and full width at half maximum (FWHM). However, considering that the surface optical path area of the microspheres covered by the cantilever and glue is less than 20%, the addition of the cantilever does not significantly affect the light field distribution and the focusing characteristics of PNJ.

3.4 Performance analysis of the customized microlens-AFM probe

The parameters of the customized microlens-AFM probe were evaluated and analyzed to ensure its performance in AFM imaging and manipulation, while maintaining the microlens' optical near-field imaging capabilities. In this study, customized microlens-AFM probes were used instead of standard commercial probes to incorporate high-resolution real-time optical imaging methods based on microlenses into AFM system. As shown in Fig. 4, the performance of the microlens-AFM probes was evaluated using the tapping mode of the AFM system. Initially, a mechanical simulation model was constructed using COMSOL multiphysics software to set the experimental parameters, and the mechanical characteristics of the microlens-AFM probe were evaluated and analyzed (Fig. 4(a)). Simulation and experimental data of characteristic frequencies of microlens-AFM probes are shown in Fig. 4(b). Both the simulated characteristic frequency and the experimentally tuned driving frequency decreased as the diameter of the coupling microlens increased. The experimental and simulation results exhibited a consistent trend with closely matching values. Different coupling positions of the microlens could also influence the characteristic frequency, leading to minor deviations. Prior to scanning imaging in tapping mode by the AFM system, it was necessary to determine the probe's inherent vibration and obtain its resonance peak through tuning. Figure 4(c) illustrates the driving frequency and amplitude of a customized microlens-AFM probe with a diameter of 60 μm. Before AFM scanning imaging, the driving frequency was set to 54.9 kHz, and the driving amplitude was set to 569.2 mV. During the scanning process, the overlap of the trace and retrace curves in the height sensor graph was observed, and the amplitude setpoint in tapping mode was adjusted until the trace and retrace scan lines were nearly consistent. The amplitude setpoint was optimized to 108.65 mV. Using this customized microlens-AFM probe, imaging of dispersed silver nanowires with a diameter of 200 nm on a silicon substrate was achieved under the aforementioned parameter settings, with a scanning speed set to 0.3 Hz and 512 scanning lines. The scan sizes were 40 μm (Fig. 4(e)) and 20 μm (Fig. 4(f)), respectively. In addition, a silver nanowire with a diameter of 80 nm was imaged, and the imaging quality of the customized microlens-AFM probe was comparable to that of a commercial probe (Figs. 4(e) and 4(i)). The cross-sectional view shows that it can effectively follow the height structure of the sample.

3.5 Observation and synchronous nanomanipulation using the customized microlens-AFM probe

Since AFM imaging relies on probe contact to capture sample morphology images, and manipulation is also achieved through probe contact, scanning imaging and manipulation cannot be

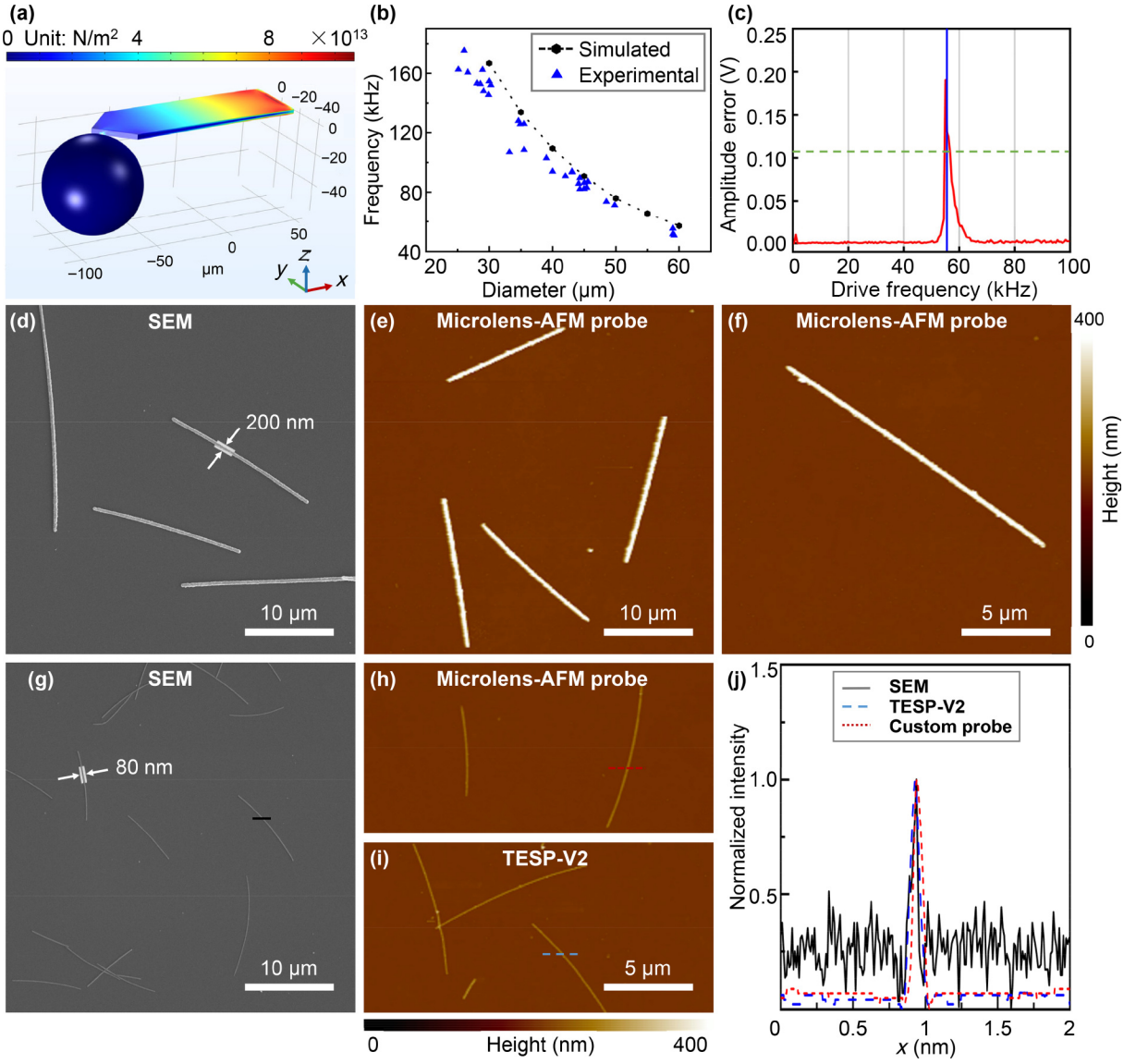

Figure 4 Analysis of AFM imaging performance of the customized microlens-AFM probe. (a) Numerical stress simulation of the microlens-AFM probe model. (b) Comparison of simulated and experimental data on characteristic frequencies of microlens AFM probes with varying diameters. (c) Adjustment of the driving frequency and amplitude for the microlens-AFM probe in tapping mode. (d) SEM images of silver nanowires with a diameter of 200 nm. (e) AFM images of 200 nm silver nanowires captured using the customized microlens-AFM probe in tapping mode. (f) AFM images of a single silver nanowire using the customized microlens-AFM probe in tapping mode. (g) SEM images of silver nanowires with a diameter of 80 nm. (h) AFM images of 80 nm silver nanowires captured using the customized microlens-AFM probe in tapping mode. (i) AFM images of 80 nm silver nanowires captured using a commercial TESP-V2 AFM probe in tapping mode. (j) Cross-section profiles along the indicated line in images (g)–(i).

performed simultaneously. Additionally, the optical microscopy resolution used for observation in AFM systems is low. To obtain morphology and position information of the hundred-nanometer sample being manipulated, determine the manipulation scheme, and evaluate the final manipulation result, the image-design-operate-image process is typically required, which results in low efficiency of nanomanipulation. We tested the manipulation and scanning imaging functions of the customized microlens-AFM probe using traditional AFM nanomanipulation processes and conducted manipulation experiments on silver nanowires with diameters of 200 and 80 nm, respectively. A microlens-AFM probe with a 60 μm diameter silica microlens and a 2 μm long diamond tip was used to scan silver nanowires with an imaging diameter of 200 nm to determine their state before manipulation. The manipulation path is indicated by the white dashed line in the figure. During the manipulation process, the probe's movement speed in the X–Y direction was set to 3 μm/s, and the deflection setting point was adjusted to 0.5 V. The stability of the manipulation process was ensured through the force control mechanism of the AFM system. To achieve targeted manipulations, the probe's X–Y movement speed and deflection setting point are calibrated beforehand. During flexing or rotation, adjustments to the nanowire's action point and torque are critical for controlled deformation. Notably, thinner nanowires (e.g., 90 nm diameter) exhibit greater bending flexibility than thicker ones (e.g., 200 nm), enabling tailored mechanical responses. Figure 5(b) shows the results of bending a 200 nm diameter silver nanowire using a microlens-AFM probe in nanoman mode. Similarly, Figs. 5(c) and

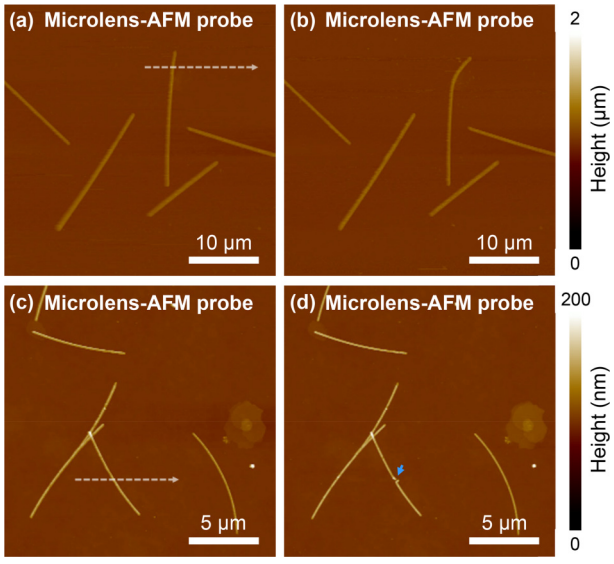

Figure 5 Manipulation of silver nanowires using a customized microlens-AFM probe. (a) and (b) Bending of silver nanowires with a diameter of 200 nm using the microlens-AFM probe in nanoman mode. (c) and (d) Cutting of silver nanowires with a diameter of 80 nm using the microlens-AFM probe in nanoman mode.

5(d) demonstrate the cutting operation of 80 nm diameter silver nanowires using a microlens-AFM probe. The scanning imaging and manipulation process of the customized microlens-AFM probe in the nanoman mode is the same as that of the commercial probe.

The optical imaging resolution of the commercial AFM system is approximately 2 μm, achieved using a 10× objective lens and a 5-megapixel camera. To address the limitations of nanoscale visual feedback in nanomanipulation technology and improve manipulation efficiency and accuracy, we designed and produced the microlens-AFM probe. By introducing a microlens-based super-resolution imaging method, we improved the imaging resolution of traditional AFM optical systems and developed a new method for nanomanipulation under the visual guidance of real-time high-resolution imaging. Figure 6 shows the results of synchronous real-time observation and manipulation of silver nanowires with a diameter of 200 nm using this method. Nanomanipulation and optical imaging were performed using the customized microlens-AFM probe with a 60 μm diameter silica microlens and a 2 μm long diamond probe tip in an AFM system. Due to the limitation of the resolution of the traditional optical imaging path in AFM, it is not possible to directly observe silver nanowires with a diameter of 200 nm to be manipulated. First, fast high-throughput scanning using microlenses can be performed before manipulation, and optical images can be stitched (Fig. 6(a)). Standard AFM imaging for observation requires scanning 256 lines to detect the position and shape of the sample before scanning. However, based on microlens scanning optical imaging, only 32 lines are needed. This approach increases imaging throughput by 8 times compared to the original imaging optical path. Moreover, the introduction of microlenses improves the optical imaging resolution, enabling real-time imaging of silver nanowires with a diameter of 200 nm. To evaluate the imaging performance of the microlens-enhanced optical imaging systems, we used a 60 μm silica microsphere integrated with the AFM's optical module to image 200 nm silver nanowires. As shown in Fig. S2 in the ESM, the microlens magnified the virtual image of the nanowires by approximately 3-fold. To quantify the system's resolution, an intensity profile was constructed by idealizing the sample information using their SEM image as a reference. This profile was then compared to a simulated optical response created by convolving the ideal intensity distribution with a Gaussian-fitting point spread function (PSF), which models the system's resolution limits. By iteratively adjusting the PSF parameters to match the experimental microlens-based images, the system's effective resolution was determined. The

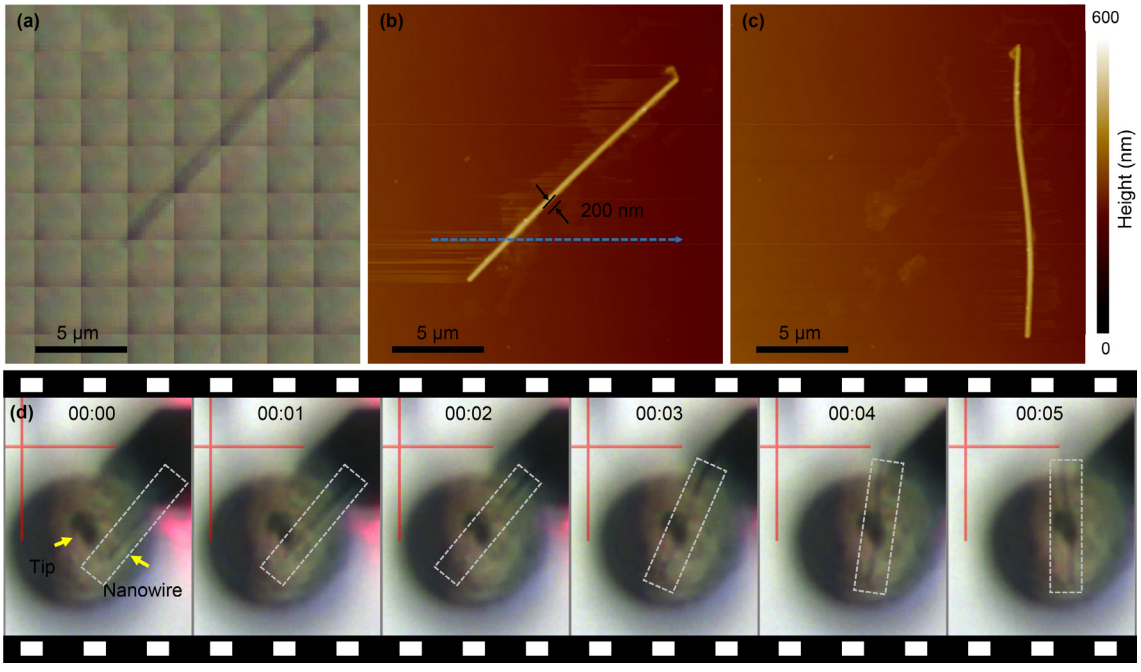

Figure 6 Observation and synchronous nanomanipulation of silver nanowires. (a) Optical stitching image of silver nanowires with a diameter of 200 nm before manipulation, obtained using a microlens. (b) AFM image of the silver nanowires with a diameter of 200 nm prior to manipulation. (c) AFM image of the silver nanowires with a diameter of 200 nm after manipulation. (d) Bending manipulation of the silver nanowire under time-efficient visual guidance based on a microlens.

FWHM of the optimized PSF revealed a resolution of approximately 650 nm for the 60 μm microlens-enhanced system.

Subsequently, under visual guidance, the silver nanowires were bent, and the tip of the AFM probe was used as the end effector during the manipulation process. The AFM system controlled the operating force, speed, and trajectory, and the microlens was coupled with the AFM optical path system to provide real-time high-resolution imaging visual guidance. During the manipulation, the manipulation situation could be observed through the microlens imaging window without the need for repeated AFM scanning imaging to check the manipulation effect (Fig. 6(d)), effectively solving the problem of lacking real-time, *in-situ*, and online visual feedback during the nanomanipulation procedure and improving the accuracy and efficiency of the nanomanipulation. A video of the manipulation process corresponding to the result shown in Fig. 6(d) is provided in Movie S1 in the ESM.

4 Conclusions

In summary, we demonstrated a time-efficient observation and synchronous nanomanipulation method leveraging a microlens for real-time visual feedback during AFM-based nanomanipulation processes. This approach involves the coupling of a microlens to the end of a conventional AFM probe cantilever, followed by the precise deposition of a diamond tip onto the microlens surface using the FIB technique. The resultant microlens-AFM probe, which we designed and fabricated, integrates microsphere-based super-resolution optical imaging technology into traditional AFM systems, achieving a notable 3× increase in imaging magnification and enhanced resolution. During nanomanipulation, the AFM probe tip served as the end effector, with the AFM system providing precise control over operating force, speed, and trajectory. The seamless integration of the microlens into the AFM optical path system facilitated real-time high-resolution imaging visual guidance, enabling the synchronous imaging and manipulation of 200 nm silver nanowires. This approach bridges the critical gap in real-time, *in-situ*, and online visual feedback during nanomanipulation, enhancing accuracy and efficiency. The microlens-AFM probe designed and manufactured in this study not only extends the functionality of traditional AFM but also demonstrates excellent compatibility with current commercial devices. Its flexibility, efficiency, and portability make it a promising tool for potential applications in the manipulation and analysis of nanoscale biological samples.

Electronic Supplementary Material: Supplementary material (Movie S1: Observation and synchronous nanomanipulation of the silver nanowire under visual guidance based on a microlens (AVI); Fig. S1: Schematic diagram illustrating the principles of imaging based on microlens; Fig, S2: Resolution estimation based on microlens-enhanced optical imaging systems (PDF)) is available in the online version of this article at https://doi.org/10.26599/NR.2025.94907397.

Data availability

All data needed to support the conclusions in the paper are presented in the manuscript and the Electronic Supplementary Material. Additional data related to this paper may be requested from the corresponding author upon request.

Acknowledgements

The authors wish to acknowledge the funding provided by the National Natural Science Foundation of China (Nos. 62074155, 62175252, and 62475279), Guangdong Basic and Applied Basic Research Foundation (No. 2024A1515012320), Shenzhen Science and Technology Innovation Commission (Nos. JCYJ20210324101405016 and JSGG20210713091807026), and China Postdoctoral Science Foundation (No. 2024M753396).

Declaration of competing interest

All the contributing authors report no conflict of interests in this work.

Author contribution statement

T. Y. Z.: Data curation, project administration, validation, investigation, methodology, experimental design, visualization, writing manuscript. H. B. Y.: Project administration, validation, experimental design. G. Q. G.: Project administration, funding acquisition. J. N. S.: Data curation. H. T. Z.: Data curation. Z. T. Y.: Data curation. S. H.: Data curation. H. Y.: Formal analysis, methodology, project administration, funding acquisition, writing – review & editing. All the authors have approved the final manuscript.

Use of AI statement

None.

References

[1] Binnig, G.; Quate, C. F.; Gerber, C. Atomic force microscope. *Phys. Rev. Lett.* **1986**, *56*, 930–933.

[2] Kim, Y.; Lieber, C. M. Machining oxide thin films with an atomic force microscope: Pattern and object formation on the nanometer scale. *Science* **1992**, *257*, 375–377.

[3] Sugimoto, Y.; Pou, P.; Custance, O.; Jelinek, P.; Abe, M.; Perez, R.; Morita, S. Complex patterning by vertical interchange atom manipulation using atomic force microscopy. *Science* **2008**, *322*, 413–417.

[4] Roos, W. H.; Wuite, G. J. L. Nanoindentation studies reveal material properties of viruses. *Adv. Mater.* **2009**, *21*, 1187–1192.

[5] Shi, H. Y.; Wang, K. X.; Tang, S.; Zhai, S. H.; Shi, J. L.; Su, C. M.; Liu, L. Q. Large range atomic force microscopy with high aspect ratio micropipette probe for deep trench imaging. *Small Methods* **2023**, *7*, 2300235 .

[6] Liu, L. Q.; Shi, J. L.; Li, M.; Yu, P.; Yang, T.; Li, G. Y. Fabrication of sub-micrometer-sized MoS_2 thin-film transistor by phase mode AFM lithography. *Small* **2018**, *14*, 1803273 .

[7] Kim, S.; Ratchford, D. C.; Li, X. Q. Atomic force microscope nanomanipulation with simultaneous visual guidance. *ACS Nano* **2009**, *3*, 2989–2994.

[8] Pennycook, S. J.; Boatner, L. A. Chemically sensitive structure-imaging with a scanning transmission electron microscope. *Nature* **1988**, *336*, 565–567.

[9] Stroscio, J. A.; Eigler, D. M. Atomic and molecular manipulation with the scanning tunneling microscope. *Science* **1991**, *254*, 1319–1326.

[10] Descloux, A.; Grußmayer, K. S.; Bostan, E.; Lukes, T.; Bouwens, A.; Sharipov, A.; Geissbuehler, S.; Mahul-Mellier, A. L.; Lashuel, H. A.; Leutenegger, M. et al. Combined multi-plane phase retrieval and super-resolution optical fluctuation imaging for 4D cell microscopy. *Nat. Photonics* **2018**, *12*, 165–172.

[11] Betzig, E.; Patterson, G. H.; Sougrat, R.; Lindwasser, O. W.; Olenych, S.; Bonifacino, J. S.; Davidson, M. W.; Lippincott-Schwartz, J.; Hess, H. F. Imaging intracellular fluorescent proteins at nanometer resolution. *Science* **2006**, *313*, 1642–1645.
[12] Bayle, V.; Fiche, J. B.; Burny, C.; Platre, M. P.; Nollmann, M.; Martinière, A.; Jaillais, Y. Single-particle tracking photoactivated localization microscopy of membrane proteins in living plant tissues. *Nat. Protoc.* **2021**, *16*, 1600–1628.
[13] Rust, M. J.; Bates, M.; Zhuang, X. W. Sub-diffraction-limit imaging by stochastic optical reconstruction microscopy (STORM). *Nat. Methods* **2006**, *3*, 793–796.
[14] Bates, M.; Huang, B.; Dempsey, G. T.; Zhuang, X. W. Multicolor super-resolution imaging with photo-switchable fluorescent probes. *Science* **2007**, *317*, 1749–1753.
[15] Vicidomini, G.; Bianchini, P.; Diaspro, A. STED super-resolved microscopy. *Nat. Methods* **2018**, *15*, 173–182.
[16] Tortarolo, G.; Zunino, A.; Fersini, F.; Castello, M.; Piazza, S.; Sheppard, C. J. R.; Bianchini, P.; Diaspro, A.; Koho, S.; Vicidomini, G. Focus image scanning microscopy for sharp and gentle super-resolved microscopy. *Nat. Commun.* **2022**, *13*, 7723.
[17] Chen, L. W.; Zhou, Y.; Li, Y.; Hong, M. H. Microsphere enhanced optical imaging and patterning: From physics to applications. *Appl. Phys. Rev.* **2019**, *6*, 021304.
[18] Wang, F. G.; Yang, S. L.; Ma, H. F.; Shen, P.; Wei, N.; Wang, M.; Xia, Y.; Deng, Y.; Ye, Y. H. Microsphere-assisted super-resolution imaging with enlarged numerical aperture by semi-immersion. *Appl. Phys. Lett.* **2018**, *112*, 023101.
[19] Li, Y. C.; Xin, H. B.; Zhang, Y.; Lei, H. X.; Zhang, T. H.; Ye, H. P.; Saenz, J. J.; Qiu, C. W.; Li, B. J. Living nanospear for near-field optical probing. *ACS Nano* **2018**, *12*, 10703–10711.
[20] Fan, W.; Yan, B.; Wang, Z. B.; Wu, L. M. Three-dimensional all-dielectric metamaterial solid immersion lens for subwavelength imaging at visible frequencies. *Sci. Adv.* **2016**, *2*, e1600901.
[21] Zhu, H. E.; Fan, W.; Zhou, S. X.; Chen, M.; Wu, L. M. Polymer colloidal sphere-based hybrid solid immersion lens for optical super-resolution imaging. *ACS Nano* **2016**, *10*, 9755–9761.
[22] Jia, B. L.; Wang, F. F.; Chan, H.; Zhang, G. L.; Li, W. J. *In situ* printing of liquid superlenses for subdiffraction-limited color imaging of nanobiostructures in nature. *Microsyst. Nanoeng.* **2019**, *5*, 1.
[23] Duan, Y. B.; Barbastathis, G.; Zhang, B. L. Classical imaging theory of a microlens with super-resolution. *Opt. Lett.* **2013**, *38*, 2988–2990.
[24] Maslov, A. V.; Astratov, V. N. Resolution and reciprocity in microspherical nanoscopy: Point-spread function versus photonic nanojets. *Phys. Rev. Appl.* **2019**, *11*, 064004.
[25] Lee, J. Y.; Hong, B. H.; Kim, W. Y.; Min, S. K.; Kim, Y.; Jouravlev, M. V.; Bose, R.; Kim, K. S.; Hwang, I. C.; Kaufman, L. J. et al. Near-field focusing and magnification through self-assembled nanoscale spherical lenses. *Nature* **2009**, *460*, 498–501.
[26] Wang, Z. B.; Guo, W.; Li, L.; Luk'Yanchuk, B.; Khan, A.; Liu, Z.; Chen, Z. C.; Hong, M. H. Optical virtual imaging at 50 Nm lateral resolution with a white-light nanoscope. *Nat. Commun.* **2011**, *2*, 218.
[27] Darafsheh, A.; Walsh, G. F.; Dal Negro, L.; Astratov, V. N. Optical super-resolution by high-index liquid-immersed microspheres. *Appl. Phys. Lett.* **2012**, *101*, 141128.
[28] Yan, Y. Z.; Li, L.; Feng, C.; Guo, W.; Lee, S.; Hong, M. H. Microsphere-coupled scanning laser confocal nanoscope for sub-diffraction-limited imaging at 25 nm lateral resolution in the visible spectrum. *ACS Nano* **2014**, *8*, 1809–1816.
[29] Yang, H.; Moullan, N.; Auwerx, J.; Gijs, M. A. M. Super-resolution biological microscopy using virtual imaging by a microsphere nanoscope. *Small* **2014**, *10*, 1712–1718.
[30] Li, L.; Guo, W.; Yan, Y. Z.; Lee, S.; Wang, T. Label-free super-resolution imaging of adenoviruses by submerged microsphere optical nanoscopy. *Light Sci. Appl.* **2013**, *2*, e104.
[31] Wang, W. C.; Yan, B.; Wang, H. Y.; Chen, Y.; Nie, X. Y.; Yi, C. F.; Wang, Z. B.; Xu, Z. S.; Zeng, J.; Fan, W. Wide-field and real-time super-resolution optical imaging by titanium dioxide nanoparticle-assembled solid immersion lens (Small 23/2023). *Small* **2023**, *19*, 2370168 .
[32] Li, J. X.; Liu, W. J.; Li, T. L.; Rozen, I.; Zhao, J.; Bahari, B.; Kante, B.; Wang, J. Swimming microrobot optical nanoscopy. *Nano Lett.* **2016**, *16*, 6604–6609.
[33] Jin, G.; Bachman, H.; Naquin, T. D.; Rufo, J.; Hou, S.; Tian, Z. H.; Zhao, C. L.; Huang, T. J. Acoustofluidic scanning nanoscope with high resolution and large field of view. *ACS Nano* **2020**, *14*, 8624–8633.
[34] Hu, X. J.; Zheng, J. J.; Zhu, Q. Q.; Wu, Q.; Li, S. S.; Yang, Y.; Chen, L. J. Acoustic assembly and scanning of superlens arrays for high-resolution and large field-of-view bioimaging. *ACS Nano* **2024**, *18*, 15218–15228.
[35] Li, Y. C.; Xin, H. B.; Liu, X. S.; Zhang, Y.; Lei, H. X.; Li, B. J. Trapping and detection of nanoparticles and cells using a parallel photonic nanojet array. *ACS Nano* **2016**, *10*, 5800–5808.
[36] Li, Y. C.; Liu, X. S.; Li, B. J. Single-cell biomagnifier for optical nanoscopes and nanotweezers. *Light Sci. Appl.* **2019**, *8*, 61.
[37] Krivitsky, L. A.; Wang, J. J.; Wang, Z. H.; Luk'yanchuk, B. Locomotion of microspheres for super-resolution imaging. *Sci. Rep.* **2013**, *3*, 3501.
[38] Zhang, T. Y.; Yu, H. B.; Shi, J. L.; Wang, X. D.; Luo, H.; Lin, D. J.; Liu, Z.; Su, C. M.; Wang, Y. C.; Liu, L. Q. Correlative AFM and scanning microlens microscopy for time-efficient multiscale imaging. *Adv. Sci.* **2022**, *9*, 2103902.
[39] Jacassi, A.; Tantussi, F.; Dipalo, M.; Biagini, C.; MacCaferri, N.; Bozzola, A.; De Angelis, F. Scanning probe photonic nanojet lithography. *ACS Appl. Mater. Interfaces* **2017**, *9*, 32386–32393.
[40] Yan, B.; Yue, L. Y.; Norman Monks, J.; Yang, X. B.; Xiong, D. X.; Jiang, C. L.; Wang, Z. B. Superlensing plano-convex-microsphere (PCM) lens for direct laser nano-marking and beyond. *Opt. Lett.* **2020**, *45*, 1168–1171.
[41] Chen, X. X.; Wu, T. L.; Gong, Z. Y.; Li, Y. C.; Zhang, Y.; Li, B. J. Subwavelength imaging and detection using adjustable and movable droplet microlenses. *Photonics Res.* **2020**, *8*, 225–234.
[42] Yan, B.; Wang, Z. B.; Parker, A. L.; Lai, Y. K.; John Thomas, P.; Yue, L. Y.; Monks, J. N. Superlensing microscope objective lens. *Appl. Opt.* **2017**, *56*, 3142–3147.
[43] Wang, F. F.; Liu, L. Q.; Yu, H. B.; Wen, Y. D.; Yu, P.; Liu, Z.; Wang, Y. C.; Li, W. J. Scanning superlens microscopy for non-invasive large field-of-view visible light nanoscale imaging. *Nat. Commun.* **2016**, *7*, 13748.